Aerodynamic Modeling for Post-Stall Flight Simulation of a Transport Airplane

N.B.Abramov[*], M.G.Goman[†]
De Montfort University (DMU), Leicester, UK, LE1 9BH

A.N.Khrabrov[‡]
Central Aerohydrodynamic Institute (TsAGI), Zhukovsky, Russia, 140160

B.I.Soemarwoto[§]
Netherlands Aerospace Centre (NLR), Anthony Fokkerweg 2, 1059 CN Amsterdam, The Netherlands

The principles of aerodynamic modeling in the extended flight envelope, which is characterized by the development of separated flow, are outlined and illustrated for a generic transport airplane. The importance of different test techniques for generating wind tunnel data and the procedure for blending the obtained experimental data for aerodynamic modeling are discussed. Complementary use of computational fluid dynamics simulations reveals a substantial effect of the Reynolds number on the intensity of aerodynamic autorotation, which is later reflected in the aerodynamic model. Validation criteria for an extended envelope aerodynamic model are discussed, and the important role of professional test pilots with post-stall flying experience in tuning aerodynamic model parameters is emphasized. The paper presents an approach to aerodynamic modeling that was implemented in the project Simulation of Upset Recovery in Aviation (2009–2012), funded by the European Union under the seventh framework programme. The developed post-stall aerodynamic model of a generic airliner configuration for a wide range of angles of attack, sideslip, and angular rate was successfully validated by a number of professional test pilots on hexapod and centrifuge-based flight simulator platforms.

Nomenclature

Re	=	Reynolds number
$\mathbf{V}, \mathbf{\Omega}$	=	linear and angular velocity vectors
V, α, β	=	flight speed, angle of attack, and sideslip angle
p, q, r	=	angular rates in body axes $OXYZ$

[*]Senior Research Fellow, School of Engineering and Sustainable Development
[†]Professor of Dynamics, School of Engineering and Sustainable Development, AIAA Senior Member
[‡]Head of Unsteady Aerodynamics Department
[§]Senior Scientist, Flight Physics and Loads Department

p_w, q_w, r_w	=	angular rates in wind axes $OX_wY_wZ_w$
$\dot{\alpha}, \dot{\beta}$	=	time derivatives of angle of attack and sideslip
$\mathbf{\Omega} = (p_w, 0, 0)'$	=	rotational velocity vector in rotary balance tests
$\omega = p_w b / 2V$	=	nondimensional wind-axis roll rate
$k = 2\pi f c / V$	=	reduced frequency of oscillations in pitch
L, M, N	=	aerodynamic moment components in body-fixed frame $OXYZ$
C_l, C_m, C_n	=	rolling, pitching and yawing aerodynamic moment coefficients,
		$L = C_l(\rho V^2/2)Sb, M = C_m(\rho V^2/2)Sc, N = C_n(\rho V^2/2)Sb$
C_N	=	aerodynamic normal force coefficient
ρ	=	air density
S	=	wing area
b	=	wing span
c	=	mean aerodynamic chord
$\delta_e, \delta_a, \delta_r$	=	elevator, aileron and rudder deflections
g	=	gravity acceleration

I. Introduction

According to worldwide commercial airplane statistics, loss of control in flight (LOC-I) is currently a major cause of flight accidents and consequent fatalities [1]. In recent years, the problem of LOC-I has been addressed from different perspectives, ranging from the use of flight simulators to teach pilots how to deal with stall and upset recovery to the development of integrated automated systems for preventing LOC-I accidents [2, 3]. The rules governing training for commercial pilots may change in the near future with the introduction of mandatory training for upset prevention and recovery. With this aim in mind, there is a need for enhanced flight simulators, first with regard to airplane aerodynamic models (specifically envelope extension to stall and post-stall conditions) and second with regard to upgraded simulator motion drive algorithms to remove limitations on simulation of airplane upsets [4].

Aerodynamic models need to be able to simulate the "g-break" phenomenon, as well as post-stall lateral-directional departures due to asymmetric development of flow separation on the airplane wing [5]. The "g-break" phenomenon is a sudden decrease of the vertical load factor following significant reduction in the aerodynamic lift coefficient provoked by symmetric flow separation over the wing. The phenomenon of wing autorotation is the result of the development of asymmetric flow separation over the wing, which is induced by angular rotation around velocity vector $\mathbf{V}$. The task of aerodynamic modeling requires the availability of suitable aerodynamic data and an appropriate structure of the aerodynamic model. Current efforts in aerodynamic modeling for transport airplanes in the extended flight envelope

[6–14] largely rely on previously established modeling principles for combat aircraft [15–18]. The latter have generally been based on the use of wind tunnel data from static, forced oscillation, and rotary balance tests [15–17], free-spin tests in vertical wind tunnels [9, 15], and large-scale free-flight model tests [19]. With some modifications, the same methodology can be applied to transport airplanes.

It is known that the maximum lift coefficient and the associated angle of attack observed in wind tunnel tests at $Re = (0.5\text{–}1.0) \times 10^6$ differ significantly from those taking place in real flight when $Re = (20\text{–}50) \times 10^6$ [19, 20]. One can expect that the aerodynamic autorotation effect due to asymmetric flow separation from both sides of the wing also depends on the Reynolds number. The latter factor provokes lateral-directional departures, adequate prediction of which is important for realistic simulation of the post-stall dynamics of an airplane. With the objective of aerodynamic modeling in the extended flight envelope, this paper pays particular attention to the computational fluid dynamics (CFD) prediction of stall aerodynamic characteristics for the NASA transport airplane configuration Common Research Model (CRM) [21, 22] using the ENFLOW CFD code, developed and validated at the Netherlands Aerospace Centre (NLR) [23, 24]. An important objective was the evaluation of the Reynolds number effect on the intensity of aerodynamic autorotation.

Post-stall aerodynamics is strongly affected by the previous history of motion of the airplane. The effect of unsteadiness of the motion is in some ways similar to that of the Reynolds number, for example, the increase in the maximum lift coefficient is proportional to the rate of change of the angle of attack $\dot{\alpha}$ [20]. To capture unsteady aerodynamic effects due to delays in the development of flow separation a number of phenomenological modeling methods have been proposed [10, 11, 25–27]. Phenomenological modeling describes empirical relationships between aerodynamic coefficients and motion parameters of the airplane. This requires appropriate formulation of the aerodynamic model structure, which does not directly follow from basic scientific principles, but describes the observed phenomenon reasonably well. For example, the importance of such phenomenological aerodynamic modeling in the stall region is discussed in [28] in terms of accuracy of the local stability characteristics in equilibrium flight conditions. A nonlinear unsteady aerodynamic modeling approach is beyond the scope of this paper, however the reader can find examples of phenomenological aerodynamic models identified using test data from wind tunnels and CFD simulation results in [11, 25, 28, 29].

Flight simulation models exploit wind tunnel data obtained using different rigs for static, forced oscillation, and rotary balance tests, but such data should be properly blended to preserve their consistency in free flight conditions. The blending procedures for a simulation with six degrees of freedom proposed in [18] were evaluated for a transport airplane [9]. The proposed procedures are accurate in developed spins, when rotation vector of the airplane $\mathbf{\Omega}$ is approximately directed along velocity vector $\mathbf{V}$, but lose fidelity in the airplane motions typical for post-stall asymmetric departures. Likewise approximate departure criteria that have been effectively used for combat aircraft [15] lose their fidelity for transport airplane configurations.

This paper presents aerodynamic modeling principles implemented in the Simulation of Upset Recovery in Aviation (SUPRA) project, funded by the 7th Framework Programme of the European Commission, Aeronautics & Transport (Aircraft Safety) [30]. The developed aerodynamic model for a generic transport airplane with two under-wing engines and a conventional tail provides representative behaviors in the extended flight envelope with inclusion of stall and post-stall conditions.

The backbone of the aerodynamic model includes experimental wind tunnel data obtained at the Central Aerohydro-dynamic Institute (TsAGI), Russia, for a typical modern transport aircraft configuration with a conventional tail [31]. The aerodynamic data were obtained in low-speed and transonic wind tunnels using different experimental facilities and test techniques. Complementary aerodynamic data were generated in CFD simulations with the objective of evaluating the effect of Reynolds number on stall aerodynamics for inclusion into the flight simulation model. The positive results of a piloted assessment of the SUPRA flight simulation model are presented in [32, 33].

II. Principles of Aerodynamic Modeling

Analysis of upset-related flight accidents shows that upset events may evolve from situations allowing safe recovery to critically dangerous and unrecoverable ones [34]. Flight safety boundaries for angle of attack, speed, or g-limit may be reached and exceeded. LOC-I and stall-related departures are possible in different phases of flight at high altitude, take-off, and landing. In piloted simulations, the aerodynamic models should adequately reflect the specific features of major nonlinear aerodynamic phenomena at high angles of attack. They should also be representative in the sense that pilots can be exposed to various scenarios associated with aircraft instability and loss of control due to stall and asymmetric flow separation.
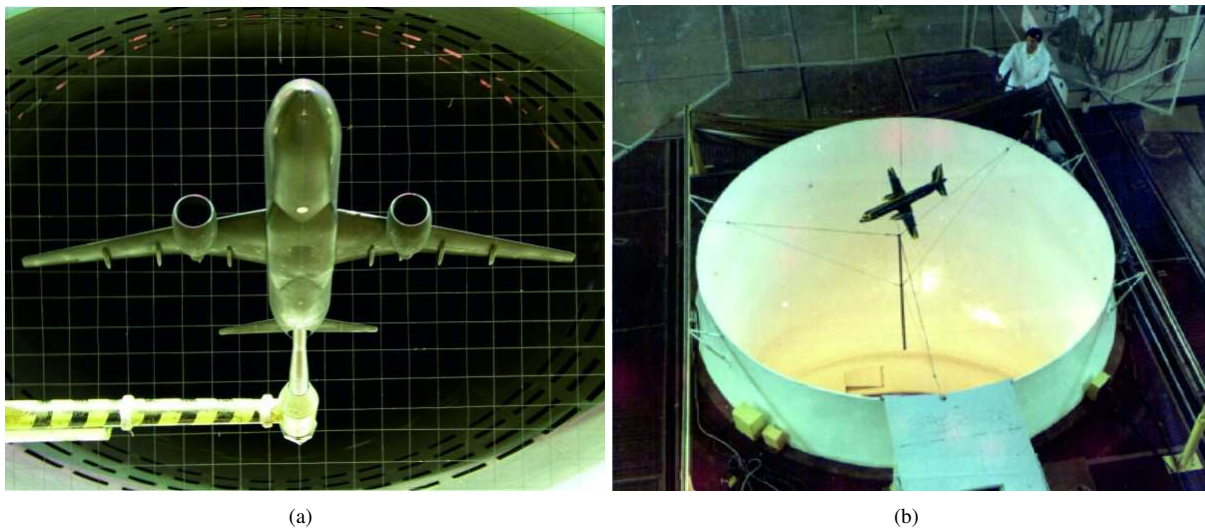

(a)   (b)

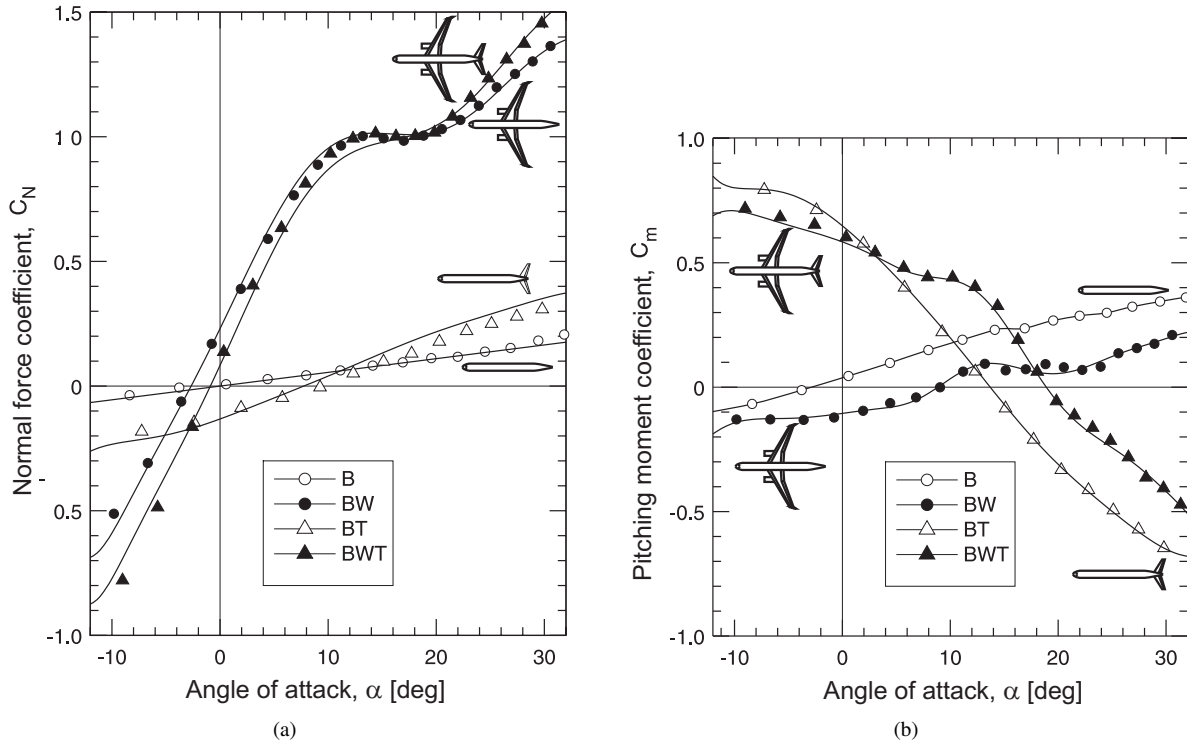Fig. 1 a) Forced oscillation rig in the TsAGI T-102 low-speed wind tunnel. b) Free-spin tests in the vertical wind tunnel T-105.

Fig. 2   Static wind tunnel data for a) normal force and b) pitching moment coefficients ($Re = 0.6 \times 10^6$, $M = 0.2$).

A. Aerodynamic Phenomena in Extended Envelope and Wind Tunnel Test Data

Various aerodynamic phenomena associated with flow separation at high angles of attack are concealed under the term "aerodynamic stall." In the post-stall region, an airplane encounters a so-called g-break effect due to an abrupt loss of lift force, and therefore simulation of this phenomenon is important for pilot training.

Among other stall-related events, there is a tendency for the onset of asymmetric rolling and yawing moments due to asymmetric flow separation, which may appear even before the maximum lift point at zero sideslip and zero rotation rate is reached. This asymmetry may be due to the high sensitivity of separated flow to imperfections in wing geometry and to contamination on the wing. Asymmetric aerodynamic moments are normally included in aerodynamic models, but there is a lack of understanding in modeling this phenomenon.

Significant changes in the dependences of aerodynamic loads compared with the static case are observed in the stall region owing to rapid changes in angle of attack or sideslip. Such dynamic stalls generate aerodynamic responses in the form of hysteresis loops, which reveal dependences on previous motion. In the case of intensive control inputs and under the action of wind gusts, an adequate modeling of stall aerodynamics in the post-stall region is essential.

Aerodynamic autorotation is another important stall-related phenomenon, caused by the action of pro-spin aerodynamic moments arising in conical motions around the velocity vector. Under post-stall conditions, these pro-spin rolling and yawing moments intensify the airplane's lateral-direction departure. A representative simulation of this
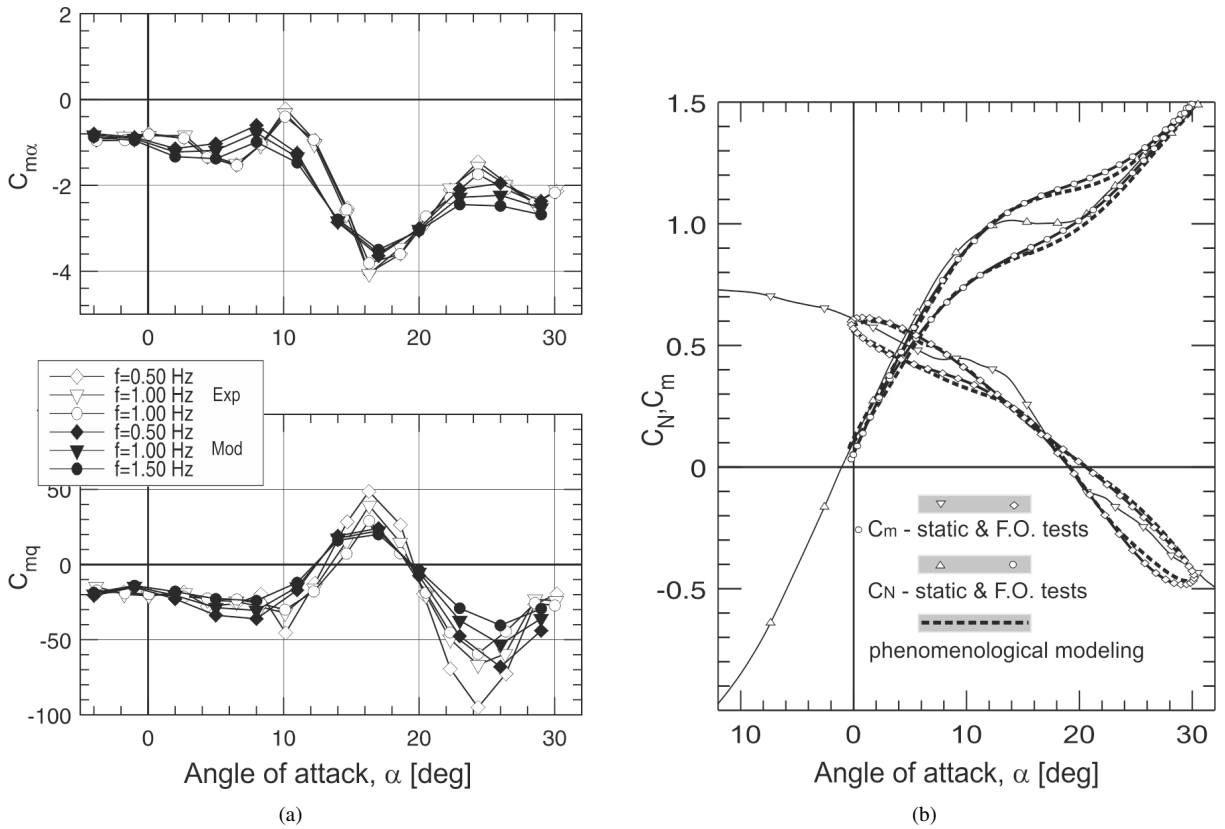
Fig. 3 Forced oscillation wind tunnel data for normal force and pitching moment coefficients ($Re = 0.6 \times 10^6$, $M = 0.2$).
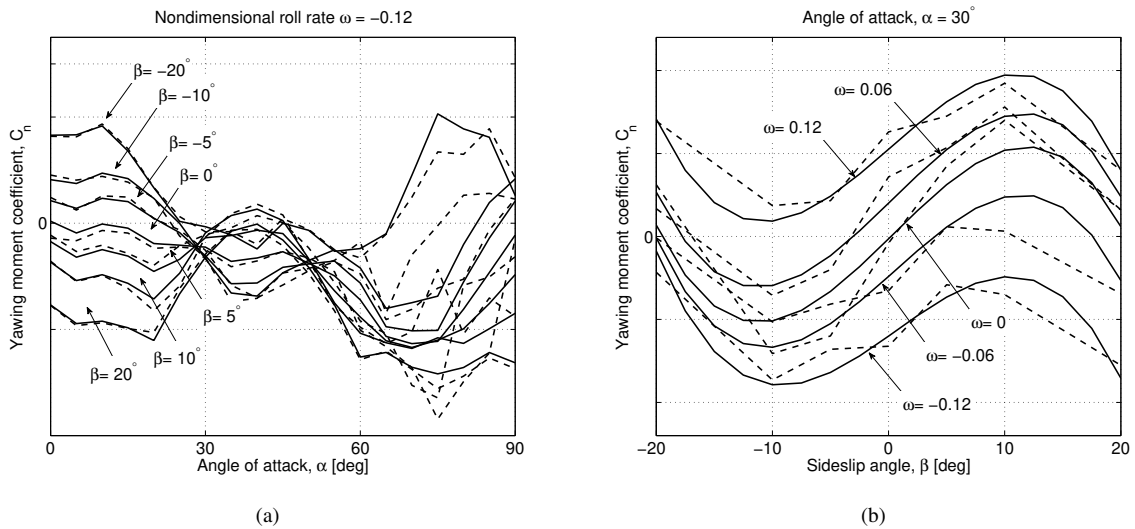

Fig. 4 Rotary balance wind tunnel data for yawing moment coefficient: dashed lines, experiment; solid lines, polynomial approximation ($Re = 0.6 \times 10^6$, $M = 0.15$).

instability is very important for positive pilot training in different phases of flight. Significant deterioration in the lateral-directional static aerodynamic derivatives in the stall region lead to adverse changes in airplane stability and controllability characteristics. High-frequency aeroelastic vibrations of the airframe due to excitation from periodic local zones of separated flow, called aerodynamic buffeting, appear in flight as a natural warning factor of the approach to stall, and therefore should be also simulated for realistic upset prevention and recovery training of pilots.

For illustrative purposes, Figs. 2– 4 show airplane models tested in wind tunnels TsAGI along with some examples of aerodynamic dependencies typical for the stall region. The forced oscillation rig with an airliner model in the T-102 low-speed wind tunnel is shown in Fig. 1a and free-spin tests with a dynamically scaled model in the T-105 vertical wind tunnel in Fig. 1b.

The dependences of the normal force and pitching moment coefficients are presented in Fig. 2 for the full airliner configuration, the body–wing–tail (BWT), along with the body–wing (BW), body–tail (BT), and body-only (B) configurations under test conditions with $Re = 0.6 \times 10^6$ and $M = 0.2$. The normal force is generated mainly on the wing, while the pitching moment is generated mainly on the tail. For the BW configuration, the normal force ceases to increase at $\alpha = 12°$ owing to aerodynamic stall on the wing, but increases again from $\alpha = 20°$ onward. In the same range of angle of attack $\alpha = 12°–20°$, the slope of the pitching moment for the BW configuration changes sign from positive to negative, and this coincides with a negative damping effect (positive values of the pitching moment derivative C_{mq} in Fig. 3a).

The rotary balance rig maintains rotation of an airplane model along the airflow velocity vector at given constant values of the angle of attack (α), sideslip (β), and nondimensional rotation rate (ω). The distributed flow conditions in such steady conical motion are kept constant, so the rotary balance can be treated as a generalized type of static tests. Typical rotary balance data obtained in the TsAGI vertical wind tunnel under conditions $Re = 0.6 \times 10^6$ and $M = 0.15$ are shown for the yawing moment coefficient $C_n(\alpha, \beta, \omega)$ by dashed lines in Fig. 4. The dependence on angle of attack for different sideslip angles at $\omega = -0.12$ is shown in Fig. 4a, and the dependence on sideslip angle for different non-dimensional rotation rates ω at $\alpha = 30°$ is shown in Fig. 4b. There is a directional instability $C_{n\beta} < 0$ in the angle-of-attack range $\alpha = 30°–50°$ (Fig. 4a).

The dependences of the yawing moment coefficient on rotary balance setting parameters α, β, ω, shown in Fig. 4, are nonlinear and not very smooth. The latter may be a consequence of big intervals in test parameters, unsteadiness of separated flow and rig vibrations (y-axis scales are removed due to the proprietary nature of data). Wind tunnel tests data are usually used in the form of multidimensional lookup tables. To generate aerodynamic dependencies as functions of motion variables the lookup tables are interpolated using piecewise-linear or smooth spline methods. An approximation of rotary balance data by a low-order polynomial function is used in the next section for blending purposes. For example, wind tunnel data shown by dashed lines in Fig. 4) are approximated by the polynomial function of third order with curves shown as solid lines. The approximation curves give reasonably accurate trends in nonlinear

variations of the yawing moment coefficient vs motion parameters α, β, ω.

Fig. 3a shows the in-phase and out-of-phase aerodynamic derivatives for the pitching moment coefficient, $C_{m\alpha}$ and C_{mq}, respectively. In the stall region $\alpha = 12°$–$20°$, the out-of-phase aerodynamic derivative C_{mq} becomes positive, indicating the onset of dynamic instability in the pitching motion. The peak instability correlates with the increased negative slope in the in-phase aerodynamic derivative $C_{m\alpha}$ (compare with the $C_m(\alpha)$ dependence for the BW configuration in Fig. 2). The variations in the normal force and pitching moment coefficients when an airplane transits through the stalled region with rapid variation of the angle of attack obtained in the forced oscillation (f.o.) tests are shown in Fig. 3b in comparison with static dependencies. In such large amplitude oscillations the use of in-phase and out-of-phase aerodynamic derivatives to predict aerodynamic responses may lose fidelity.

B. Blending Wind Tunnel Aerodynamic Data

The accuracy of six-degree-of-freedom (6-DOF) simulation depends on how data from different tests in a wind tunnel are incorporated into the aerodynamic model. The static, forced oscillation, and rotary balance tests are conducted with different setting conditions, and this should be taken in account when blending data from these tests.

Methods for blending of rotary balance and forced oscillation test data, proposed in [18] for fighter configurations, were evaluated in [9] for a transport airplane configuration. They give good predictions of the parameters of steady developed spins, when the airplane rotation is dominant along the velocity vector **V**, but fail for the transitional dynamics typical of post-stall lateral-directional departures and agitated oscillatory spins.

In an equilibrium, flight aerodynamic responses due to disturbed motion in pitch, roll, and yaw are commonly described as increments towards the aerodynamic loads measured in static wind tunnel tests. These increments are introduced in the form of linear terms, with the unsteady and rotary aerodynamic derivatives being determined experimentally in small-amplitude forced oscillation tests. The following equations for the aerodynamic coefficients include nonlinear dependences on angle of attack, sideslip, and control surface deflections, obtained from static wind tunnel tests, and incremental linear contributions defined by unsteady aerodynamic derivatives:

$$C_l = C_l^{\text{st}}(\alpha, \beta, \delta_a, \delta_r) + C_{l_p}^{\text{f.o.}} \frac{pb}{2V} + C_{l_r}^{\text{f.o.}} \frac{rb}{2V},$$

$$C_m = C_m^{\text{st}}(\alpha, \beta, \delta_e) + C_{m_q}^{\text{f.o.}} \frac{qc}{V}, \tag{1}$$

$$C_n = C_n^{\text{st}}(\alpha, \beta, \delta_a, \delta_r) + C_{n_p}^{\text{f.o.}} \frac{pb}{2V} + C_{n_r}^{\text{f.o.}} \frac{rb}{2V}.$$

Here the forced oscillation (f.o.) aerodynamic derivatives $C_{i_j}^{\text{f.o.}}$ ($i = l, m, n$; $j = p, q, r$) accumulate an aggregated effect from simultaneous variation of p, q, r and $\dot{\alpha}, \dot{\beta}$ owing to the following kinematic coupling in rotation around a fixed

point:

$$\dot{\alpha} = q - (p \cos \alpha + r \cos \alpha) \tan \beta,$$

$$\dot{\beta} = -p \sin \alpha + r \cos \alpha. \tag{2}$$

The aggregates of rotary and unsteady aerodynamic derivatives can be calculated using the following equations:

$$C_{i_p}^{\text{f.o.}} = C_{i_p} + C_{i_\beta} \sin \alpha - \frac{2c}{b} C_{i_{\dot\alpha}} \cos \alpha \tan \beta,$$

$$C_{i_r}^{\text{f.o.}} = C_{i_r} - C_{i_\beta} \cos \alpha - \frac{2c}{b} C_{i_{\dot\alpha}} \sin \alpha \tan \beta, \tag{3}$$

$$C_{i_q}^{\text{f.o.}} = C_{i_q} + C_{i_{\dot\alpha}}, \quad i = l, m, n.$$

In post-stall asymmetric departures and developed spin modes, the motion of an airplane can be described as a perturbed conical rotation about linear velocity vector $\mathbf{V}$. The intensity of conical rotation and its perturbations can be defined by projections of the angular velocity vector $\mathbf{\Omega}$ in the wind-axis reference frame, p_{w}, q_{w}, and r_{w} (Fig. 5):

$$\begin{vmatrix} p_{\text{w}} \\ q_{\text{w}} \\ r_{\text{w}} \end{vmatrix} = \begin{bmatrix} \cos \alpha \cos \beta & \sin \beta & \sin \alpha \cos \beta \\ -\cos \alpha \sin \beta & \cos \beta & -\sin \alpha \sin \beta \\ -\sin \alpha & 0 & \cos \alpha \end{bmatrix} \begin{vmatrix} p \\ q \\ r \end{vmatrix}, \tag{4}$$

where p, q, and r are respectively the roll, pitch, and yaw rates in the body-axis reference frame. In pure conical rotation,
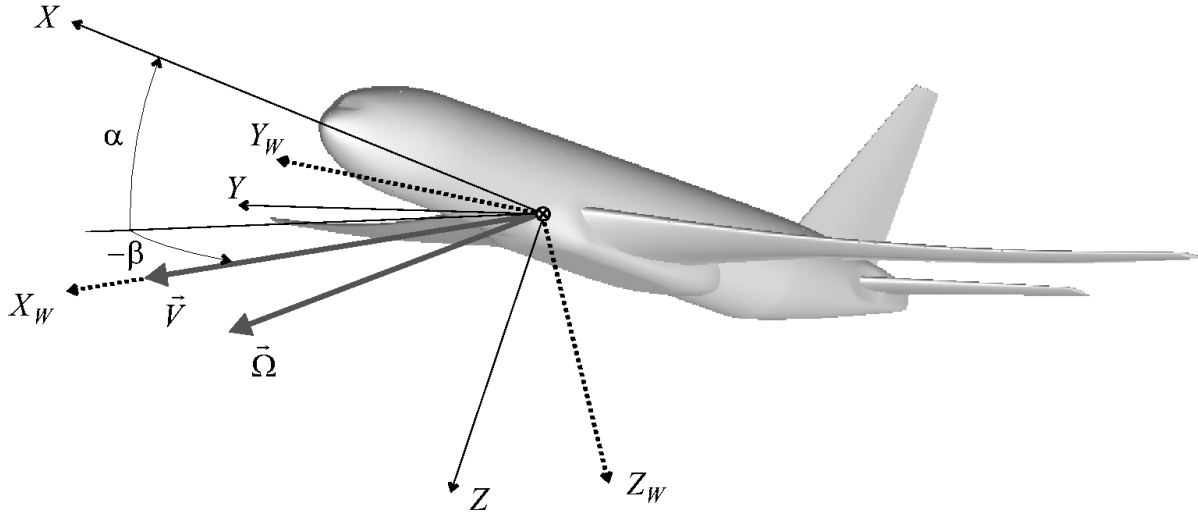

Fig. 5   Body-axis and wind-axis reference frames.

the wind-axis angular rates in pitch and yaw projections disappear ($q_{\text{w}} = r_{\text{w}} = 0$), while p_{w} can be identified with the

nondimensional rate of conical rotation ω, which is used as a parameter in the rotary balance tests. It is natural to treat the rates q_w and r_w as perturbation parameters for pure conical rotation, and they should be substantially smaller than the conical rotation rate: $|q_w/p_w| \ll 1$, $|r_w/p_w| \ll 1$. From Eqs. (2) and (4) there follows a direct connection between these angular rates and the intensity of changes in the angle of attack and sideslip: $\dot{\alpha} = q_w/\cos\beta$ and $\dot{\beta} = r_w$.

For conical-like rotations, the aerodynamic coefficients can be represented in a similar manner to Eqs. (1), but with static test data replaced by rotary balance (r.b.) test data with incremental aerodynamic responses, which are now proportional to q_w and r_w:

$$C_l = C_l^{\text{r.b.}}(\alpha, \beta, \omega, \delta_a, \delta_r) + C_{l_{qw}} \frac{q_w c}{V} + C_{l_{rw}} \frac{r_w b}{2V},$$

$$C_m = C_m^{\text{r.b.}}(\alpha, \beta, \omega, \delta_e) + C_{m_{qw}} \frac{q_w c}{V} + C_{m_{rw}} \frac{r_w b}{2V}, \tag{5}$$

$$C_n = C_n^{\text{r.b.}}(\alpha, \beta, \omega, \delta_a, \delta_r) + C_{n_{qw}} \frac{q_w c}{V} + C_{n_{rw}} \frac{r_w b}{2V}.$$

where aerodynamic derivatives C_{i_j} ($i = l, m, n$; $j = p_w, q_w, r_w$) correspond to conditions of conical motion and therefore depend on the nondimensional rotation rate ω.

The nonlinear rotary balance terms in Eqs. (5) are well approximated by third- or fifth-order polynomial functions with respect to the sideslip angle β and the nondimensional rotation rate ω (see Fig. 4):

$$C_i^{\text{r.b.}}(\alpha, \beta, \omega) = C_{i0}(\alpha) + C_{i_\beta}^{\text{r.b.}}(\alpha)\beta + C_{i_\omega}^{\text{r.b.}}(\alpha)\omega$$

$$+ C_{i_{\omega^2}}(\alpha)\omega^2 + C_{i_{\beta\omega}}(\alpha)\beta\omega + C_{i_{\beta^2}}(\alpha)\beta^2 \tag{6}$$

$$+ C_{i_{\omega^3}}(\alpha)\omega^3 + C_{i_{\beta^2\omega}}(\alpha)\beta^2\omega + C_{i_{\beta\omega^2}}(\alpha)\beta\omega^2 + C_{i_{\beta^3}}(\alpha)\beta^3, \quad i = l, m, n.$$

At small β and ω, the following relations between the forced oscillation and rotary balance aerodynamic derivatives can be established:

$$C_{i_{p_w}}(\alpha) = C_{i_\omega}^{\text{r.b.}}(\alpha) = C_{i_p}^{\text{f.o.}}(\alpha)\cos\alpha + C_{i_r}^{\text{f.o.}}(\alpha)\sin\alpha, \quad i = l, n,$$

$$C_{i_{r_w}}(\alpha) = -C_{i_p}^{\text{f.o.}}(\alpha)\sin\alpha + C_{i_r}^{\text{f.o.}}(\alpha)\cos\alpha, \quad\quad i = l, n, \tag{7}$$

$$C_{m_{q_w}}(\alpha) = C_{m_q}^{\text{f.o.}}(\alpha), \quad\quad C_{m_{p_w}}^{\text{r.b.}} = C_{l_{q_w}}^{\text{r.b.}} = C_{n_{q_w}}^{\text{r.b.}} = 0.$$

According to Eqs. (6) and (7), the rotary balance unsteady aerodynamic derivatives can be estimated and used in Eqs. (5) with data from rotary balance tests. Such a blending fits well for post-stall lateral-directional departures, but may fail to correctly predict dynamic stability in agitated spins, because of differences in flow conditions. Note that the unsteady aerodynamic derivatives are obtained in the forced oscillation tests without the steady conical rotation typical of spin motion. Additional experimental capabilities are required for improvement of unsteady aerodynamic modeling.

For example, the oscillatory coning technique [35] provides more appropriate testing conditions for extraction of the unsteady aerodynamic derivatives $C_{i_{q_\mathrm{w}}}$ and $C_{i_{r_\mathrm{w}}}$ in Eqs. (7). A wind tunnel 5-DOF dynamic rig [36] allowing execution of free lateral-directional departures can be used for identification of aerodynamic characteristics under unsteady stall conditions.

III. Complementary Use of CFD Simulations

CFD simulations were used for validation of experimental data in the stall region with the particular objective of extrapolating data to high-Reynolds-number conditions [13, 14]. Static and dynamic tests in wind tunnels are normally conducted at relatively low Reynolds numbers ($Re \approx 1 \times 10^6$), with CFD methods allowing predictions of aerodynamic loads at the higher Reynolds numbers ($Re = 50 \times 10^6$ in this paper) typical of real flight conditions. CFD methods using numerical procedures specially tuned for separated flow conditions can be used for prototyping wind tunnel tests typical of static conditions and forced oscillation tests as presented in [11, 29]. This section presents CFD simulations of aerodynamic loads during rotary balance tests, which are of great importance for satisfactory aerodynamic modeling in the extended flight envelope.

A. CFD Computational Framework

For evaluation of the wing autorotation effect, a body–wing configuration of the NASA CRM geometry [21, 22], typical of many modern transport airplanes, was considered. Both the coarse and medium grids used in this study, containing 5.1 or 10.2 million grid cells, respectively, were obtained from [21, 37]. To allow efficient parallel processing on the high-performance cluster computing facility at NLR, the grid was divided into 156 blocks, allowing an almost perfectly balanced parallel computation using 160 cores with 80 MPI domains. The unified grid was designed for $Re = 5 \times 10^6$. To provide sufficient resolution of the turbulent boundary layer with y^+ values on the surface close to unity, a special procedure was applied to redistribute the original grid within the boundary layer. This procedure allowed flow simulations with much higher Reynolds numbers up to 50×10^6.

The NLR's CFD code ENFLOW used in this study has, since its inception [23], been continuously developed in-house to incorporate new capabilities ranging from Reynolds-averaged Navier–Stokes (RANS) with increasing fidelity of the turbulence model, to unsteady RANS (URANS), to hybrid RANS/large-eddy simulation (LES) and LES. The ENFLOW solution algorithm can be found in [24]. The ENFLOW steady-state numerical solution for the NASA CRM drag polar agrees well with available experimental results: it is well within the CFD and wind-tunnel spreads, and is absolutely not an outlier. A flow model based on the URANS equations was used in this paper throughout the simulations, along with Menter's shear stress transport (SST) turbulence model [38].

A conical roll motion around the incoming free-stream velocity vector was considered as a representative case for simulation of post-stall departure. This type of motion is identical to that in the rotary balance tests, but a CFD

simulation is free from wind tunnel interference effects and can be applied at high Reynolds numbers. The conical motion is characterized by constant kinematic parameters, angle of attack α, sideslip β, and rotation rate ω, ensuring steady conditions for local flow incidences. In the CFD model, the conical roll-motion is modeled by rotating the computational grid, where the free-stream velocity vector is used as the axis of rotation, and the moment reference point as the center of rotation.

Before a fully fledged campaign for generation of aerodynamic data, a validation study was performed to determine the most appropriate balance between spatial resolution and required computing resources. A second-order implicit scheme with dual time-stepping is used to simulate the roll-motion. A non-dimensional time step size of 0.2 was chosen to allow 10 samples per period. It was immediately clear that time-accurate simulations on the fine grid were practically not feasible. The medium grid alleviates the situation but still requires tremendous computational resources. An investigation was therefore performed to find out whether using a less expensive coarse grid was justifiable. Three cases were evaluated: (a) steady-state simulation on the coarse grid, (b) time-accurate simulation on the coarse grid, and (c) time-accurate simulation on the medium grid. At low angles of attack with attached flow conditions, all three approaches gave identical results. In regimes with flow separation, the steady-state solution procedure, although having modest computational requirements, was not able to reach convergence. The force and moment coefficients were approximated through a reasonable averaging of the fluctuating coefficients. The time-accurate simulation required more computational time and allowed meaningful convergence to nearly steady flow solutions.

For the CRM wing–body configuration in conical motion at $M = 0.4$, $Re = 5 \times 10^6$, and $\omega = 0.1$, three sample dependences of the pitching and rolling moment coefficients C_m and C_l versus angle of attack in the range $2° < \alpha < 16°$ were simulated using different grids and computational methods (Fig. 6). Comparative analysis of these results, revealing differences in the distributions of flow separation, led to the conclusion that the medium grid with time-accurate simulation was the best setting for further computational testing.

The final computational procedure for flow simulation for each set of α, β, ω was conducted independently in parallel and in two stages, and started from a free stream as the initial flow. In the first stage, a grid sequencing procedure was followed, using a steady-state simulation involving three grid levels. For a roll motion in the wind axis, the steady-state solution procedure was based on the steady-state RANS equations formulated in the rotating body-axis reference frame.

In the second stage, the computational procedure was switched to a time-accurate simulation. After 320 nondimensional physical time steps of $\tau = 0.2$, the transient process had decayed sufficiently, and the force and moment aerodynamic coefficients could be extracted by averaging over an appropriate number of periods of oscillation.

Figure 7 shows the simulation processes on the medium grid for the normal force and rolling moment coefficients at $\alpha = 14°$, $\omega = 0.1$ and at $\alpha = 40°$, $\omega = 0.1$.

The processes converge to periodic solutions exhibiting high-frequency oscillations with small amplitude, which are more pronounced at $\alpha = 40°$. It should be noted that in several cases engineering judgement was needed in order

to obtain acceptable numerical figures within the available resources. This situation is reflected in Fig. 7 where the roll-motion coefficient had not yet fully converged.

The eCFD framework, using an e-mail interface, allowed planning and execution of the required numerical simulations at De Montfort University, UK, benefiting from the high-end CFD software and hardware infrastructure at NLR [39]. The large number of flow simulations required for the aerodynamic model in the extended flight envelope were performed in parallel. For example, one unsteady flow simulation took about 3 hours and 45 minutes. The shared computing facility at NLR allowed a production capacity of 18 simulations per day.
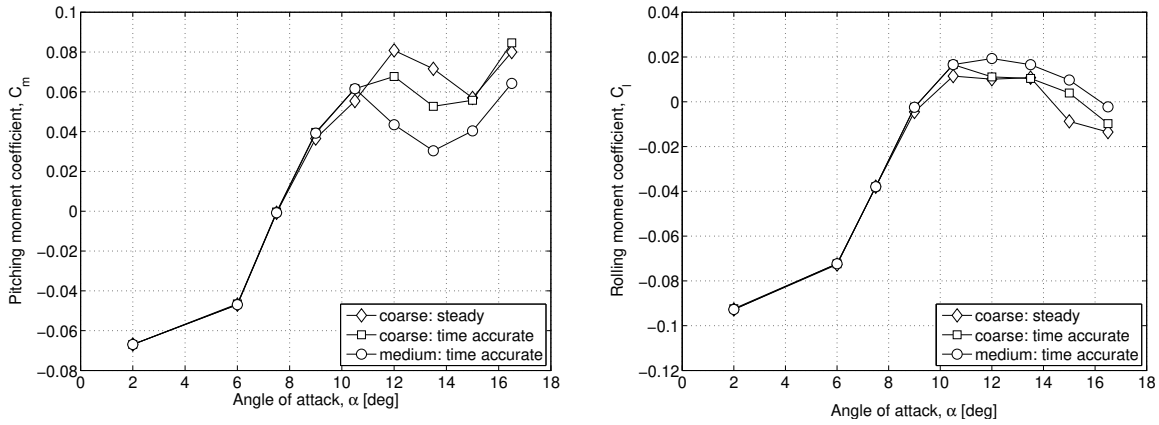
Fig. 6 **Effects of grid and solution procedure on aerodynamic moment coefficients at $M = 0.4$, $Re = 5 \times 10^6$, and $\omega = 0.1$ for a CRM body–wing configuration.**
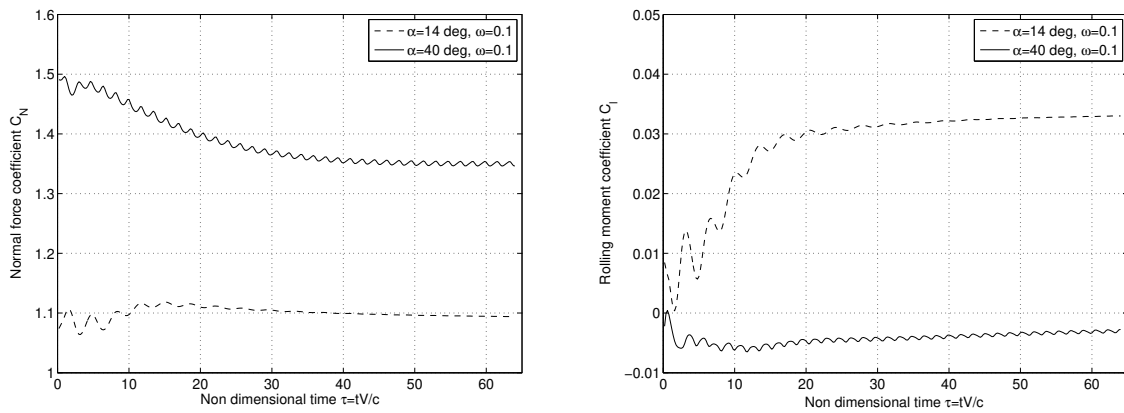
Fig. 7 **Convergence process in a time-accurate simulation, the second stage in a two-stage procedure for generating aerodynamic data in the post-stall region: $M = 0.2$, $Re = 32.6 \times 10^6$, $\omega = 0.1$, and $\alpha = 14°$ and $40°$.**

B. CFD of Rotary Balance Testing

CFD simulations were conducted at $M = 0.2$ and two different Reynolds numbers $Re = 1.0 \times 10^6$ and 32.6×10^6 for the CRM body–wing configuration on a grid of points for angle of attack α and nondimensional conical roll rate ω
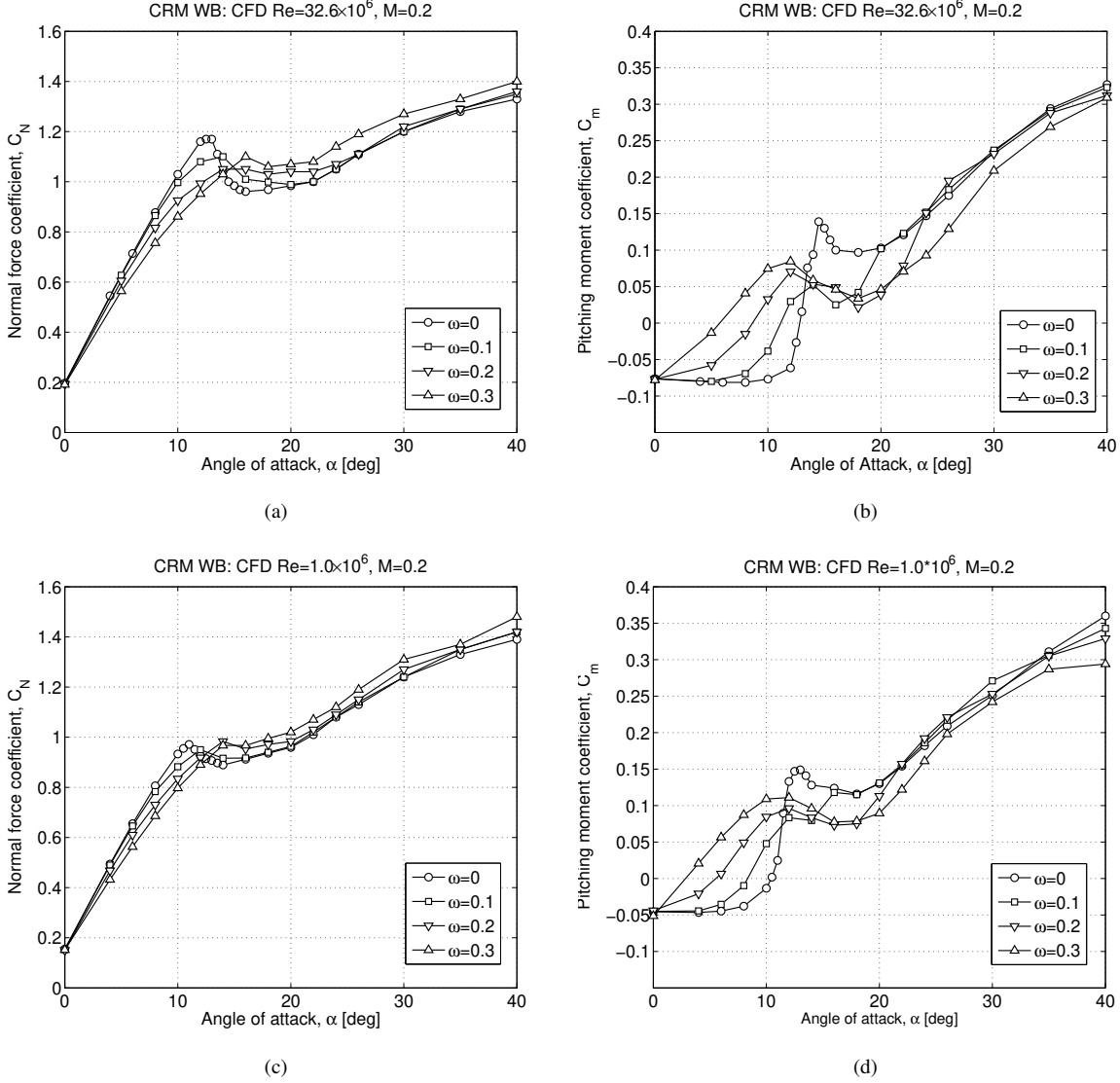
Fig. 8 **CFD simulation results for normal force and pitching moment coefficients for CRM body–wing config-**
uration in conical motion: a, b) at $Re = 32.6 \times 10^6$; c, d) $Re = 1.0 \times 10^6$.

at zero sideslip $\beta = 0$. This allowed the production of dependences of the force and moment coefficients in the stall

region similar to those obtained in the wind tunnel rotary balance tests.

The normal force $C_N(\alpha, \omega)$ and pitching moment $C_m(\alpha, \omega)$ coefficients generated in CFD simulations are presented

in Fig. 8. These dependences at $Re = 1.0 \times 10^6$ and 32.6×10^6 are qualitatively similar, but there are some important

quantitative differences, especially in the stall region. For example, $C_N(0,0) = 0.152$ and $C_{N_{\max}}(11°, 0) = 0.971$ at

$Re = 1.0 \times 10^6$, while $C_N(0,0) = 0.191$ and $C_{N_{\max}}(13°, 0) = 1.17$ at $Re = 32.6 \times 10^6$. At high Reynolds number, the

maximum value of the normal force coefficient is increased ($\Delta C_{L_{\max}} \approx 0.19$), is shifted to a higher angle of attack

($\Delta \alpha_{\max} \approx 2°$), and is followed by a steeper drop in magnitude. Similar quantitative changes occur in the pitching moment

coefficient. For example, $C_m(0,0) = -0.046$ and $C_{m_{\max}}(13°,0) = 0.15$ at $Re = 1.0 \times 10^6$, while $C_m(0,0) = -0.0781$ and $C_{m_{\max}}(14.5°,0) = 0.149$ at $Re = 32.6 \times 10^6$. At high Reynolds number, there is a steeper drop in the pitching moment coefficient above $\alpha = 14.5°$, potentially leading to an increase in the peak of negative damping at high Reynolds number in comparison with the wind tunnel test data obtained at low Reynolds number (see the range $\alpha = 14°$–$18°$ in Fig. 3a).

Flow visualizations for symmetric conditions at $Re = 32.6 \times 10^6, M = 0.2$ are shown in Fig. 9. The surface limiting streamlines with a skin-friction pattern in the background for a number of angles of attack $\alpha = 12°, 14°, 16°, 30°$, at $\beta = \omega = 0$, are shown in Fig. 9a. Areas with relatively low skin friction indicate regions with flow separation. At $\alpha = 12°$, the streamlines show that the flow is attached to the wing, but at higher angles of attack the streamlines indicate flow separation with a pattern changing with increasing angle of attack. The distribution of Mach number at $\alpha = 12°, \omega = 0$ (attached flow) and at $\alpha = 14°, \omega = 0$ (separated flow) in the cross-section of the mean aerodynamic chord on the starboard wing is shown in Fig. 9b. Two circulatory regions of opposite rotation on both wing sides appear at $\alpha = 14°$, revealing the existence of two vortical flow separations from the upper wing surface. With increasing angle of attack, these circulatory regions approach the fuselage and disappear. The spatial evolution and topology of these vortices require further investigation.

The effect of conical rotation in the stall region is illustrated in Fig. 10. On the left-hand image in Fig. 10a, the limiting streamlines clearly show separated flow over the wing surface at $\alpha = 12°$ and zero rotation. The starboard-down roll motion inducing a higher local angle of attack on the starboard side is consistent with the greater extent of the flow separation region on that side and the attached flow on the port side of the wing. Figure 10b shows the pressure coefficient and Mach number contours at the location of the mean aerodynamic chord for the port side with attached flow and the starboard side with separated flow. These asymmetric flow conditions during starboard-down conical rotation generate pro-spin aerodynamic moments, leading to autorotation instability.

The predicted aerodynamic moment coefficients $C_l(\alpha, \omega)$ and $C_n(\alpha, \omega)$ are presented in Fig. 11. At low angles $\alpha < 10°$, the rolling and yawing moment derivatives are negative, $C_{l\omega} < 0$ and $C_{n\omega} < 0$, and this contributes to the lateral-directional stability. In the stall region, there is a strong nonlinear dependence on the conical non-dimensional rotation rate ω. At low rotation rates $\omega < 0.1$, in the range $12° < \alpha < 20°$, the rolling and yawing moment derivatives change sign and become positive, $C_{l\omega} > 0$ and $C_{n\omega} > 0$ (solid lines in Fig. 11). However, with increasing rotation rate $\omega > 0.1$, the slopes of the curves change back to negative values, $C_{l\omega} < 0$ and $C_{n\omega} < 0$, and cross the zero levels, $C_l = 0$ or $C_n = 0$, at some values of ω.

The rolling moment derivative $C_{l\omega}$ for the CRM body–wing configuration obtained in CFD simulations is shown in Fig. 12a. The intensity of aerodynamic autorotation ($C_{l\omega}$) increases with increasing Reynolds number. The peak negative damping at $Re = 32.6 \times 10^6$ is delayed by $2°$ in angle of attack and is doubled in magnitude in comparison with the corresponding dependence for $Re = 1.0 \times 10^6$. The aerodynamic derivatives $C_{l\omega}$ and $C_{n\omega}$ in conical motion can be evaluated from the wind tunnel rotary balance or forced oscillation tests. Figure 12b shows the rolling moment
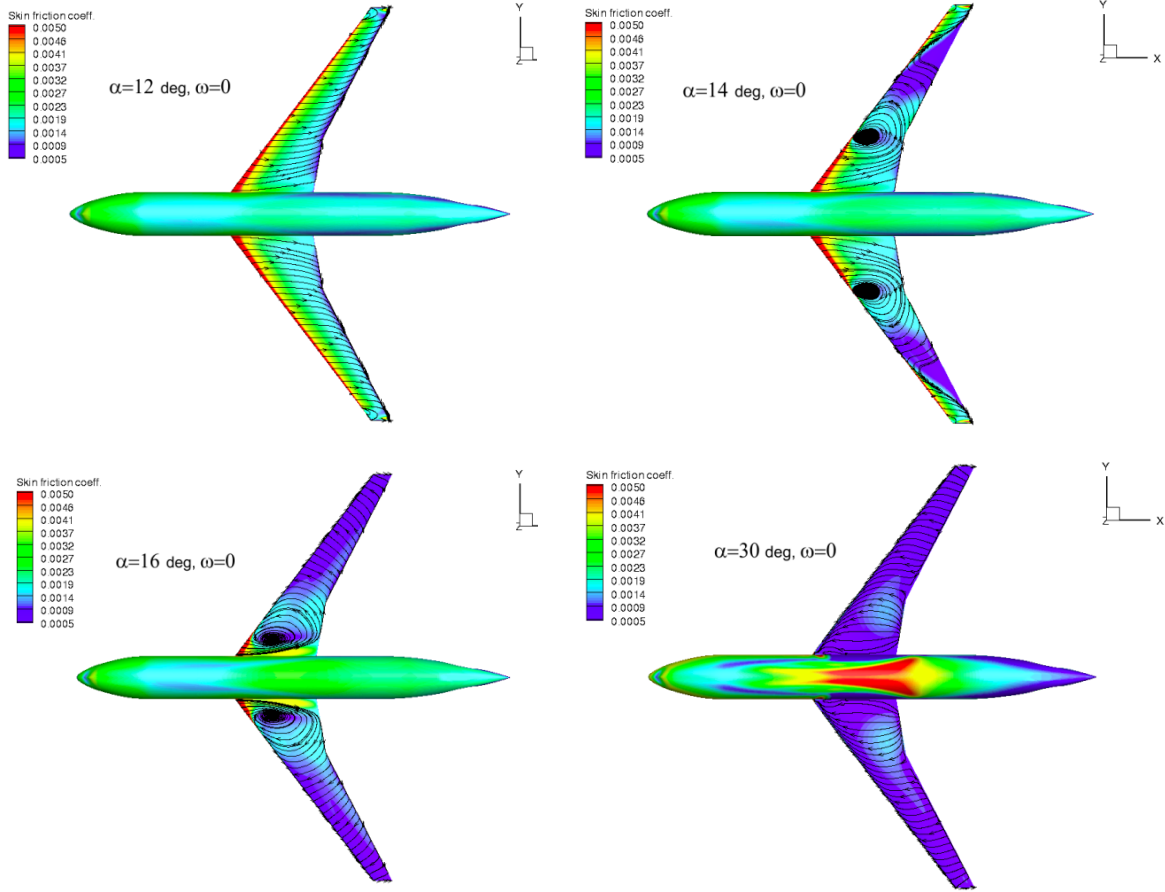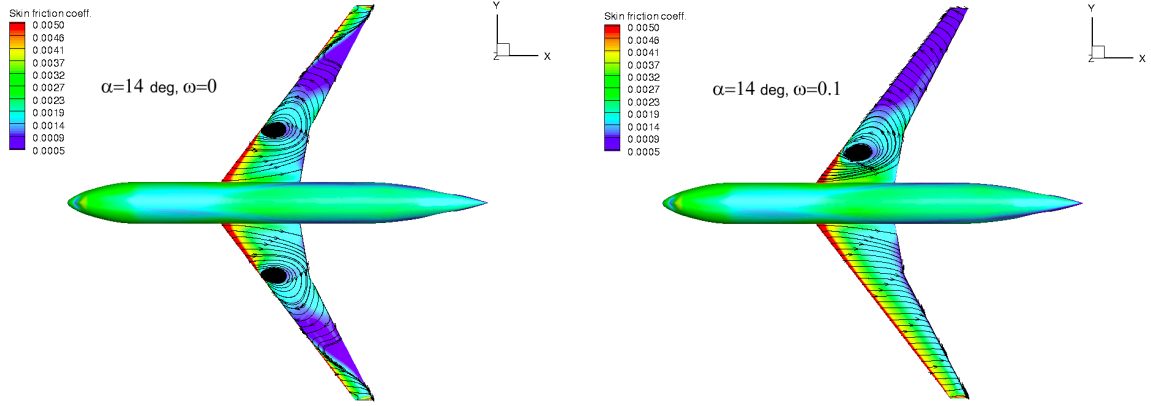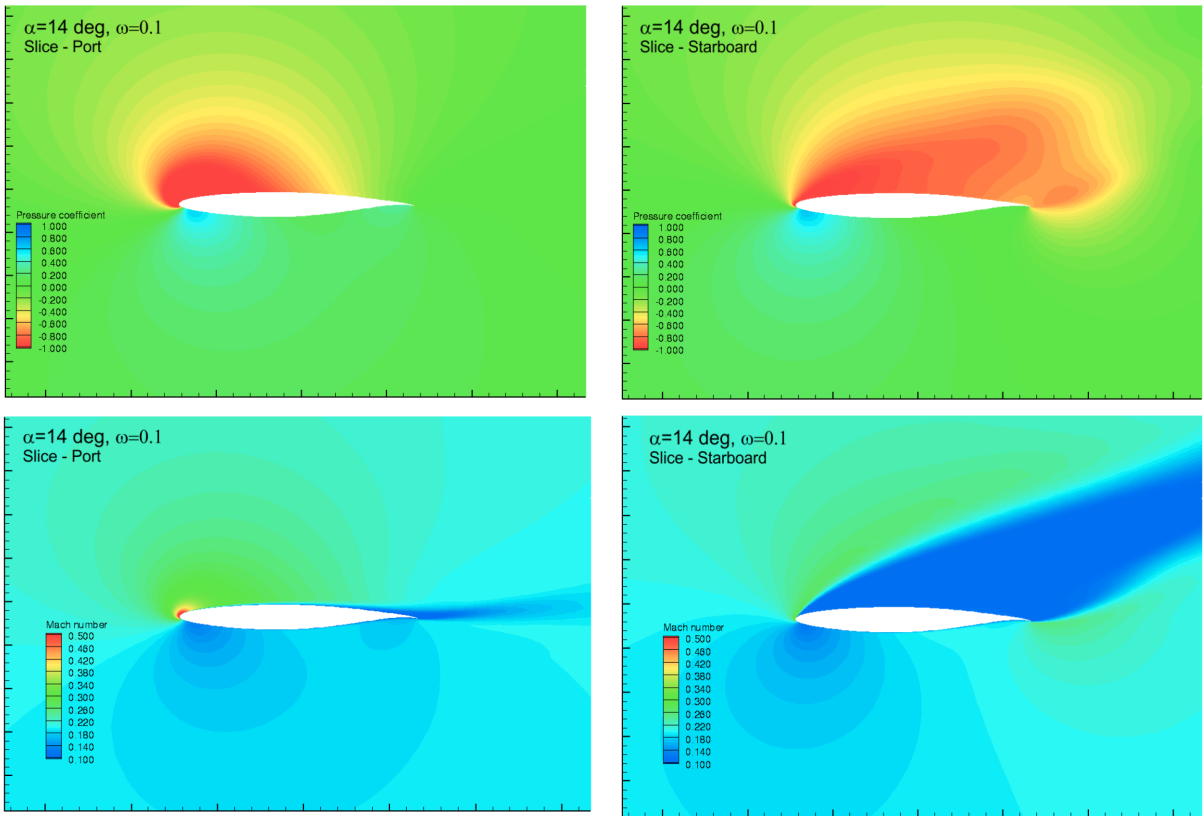
(a)
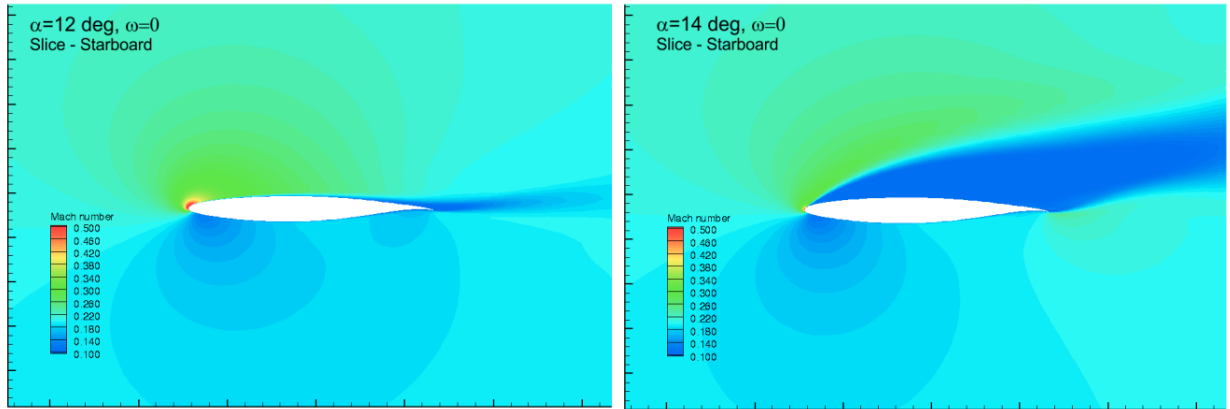
(b)

Fig. 9   Flow visualization. a) Surface limiting streamlines with skin-friction pattern in the background for $\alpha = 12°, 14°, 16°, 30°$ at $\omega = 0$. b) Mach number distribution at the location of the mean aerodynamic chord on the starboard wing at $\alpha = 12°$, $\omega = 0$ and $\alpha = 14°$, $\omega = 0$.

derivative $C_{l\omega}$ (solid line) calculated with the first of Eqs. (7), using the aerodynamic derivatives $C_{lp}^{\text{f.o.}}$ and $C_{lr}^{\text{f.o.}}$ (dashed lines) obtained for the SUPRA configuration in the wind tunnel forced oscillation tests with $Re = 0.6 \times 10^6$. Under these

(a)

(b)

Fig. 10 Flow visualization. a) Surface limiting streamlines with skin-friction pattern in the background for $\alpha = 14°, \omega = 0$ and $\alpha = 14°, \omega = 0.1$. b) Pressure and Mach number distributions at the location of the mean aerodynamic chord at $\alpha = 14°, \omega = 0.1$ on the port and starboard sides.

conditions, all three dependences $C_{l\omega}$, $C_{lp}^{\text{f.o.}}$, and $C_{lr}^{\text{f.o.}}$ clearly show that the level of damping in conical rotation drops to zero at $\alpha = 14°$, and there is no autorotation effect in the whole post-stall region. This means that the intensity of the aerodynamic autorotation observed in wind tunnel tests at low Reynolds numbers may be significantly undervalued or
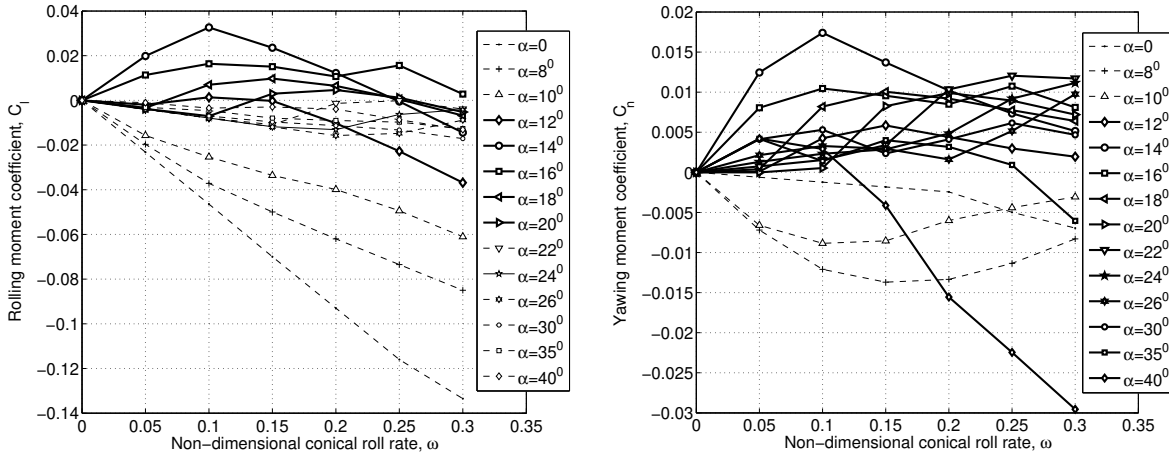
Fig. 11 CFD simulation results for rolling and yawing moment coefficients of the CRM body–wing configuration in conical motion at $Re = 32.6 \times 10^6$ and $M = 0.2$.

totally missed in comparison with the level of aerodynamic autorotation in real flight conditions.

The presented results of the CFD simulations demonstrate a significant level of aerodynamic autorotation in the stall region at low and high Reynolds numbers, and therefore a proper account of this effect is of great importance for aerodynamic modeling. A similar observation regarding the relation between wind tunnel forced oscillation test data and CFD predictions was reported in [11] for the aerodynamic derivative $C_{lp}^{\text{f.o.}}$ of the generic transport model (GTM) configuration.
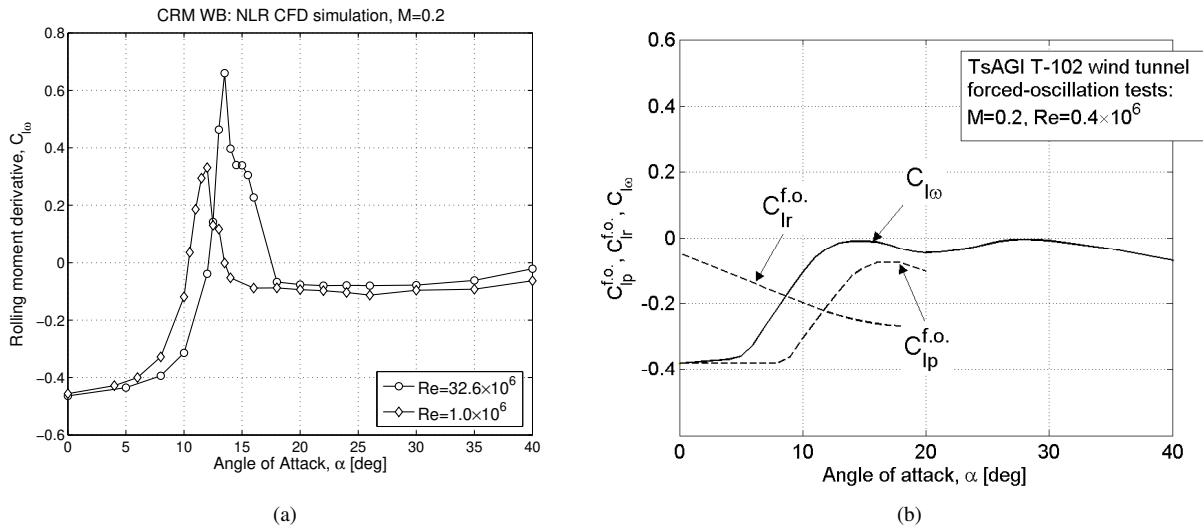

Fig. 12 a) Rolling moment derivative $C_{l\omega}$ obtained from CFD simulations at $Re = 1 \times 10^6$ and 32.6×10^6. b) Rolling moment derivative $C_{l\omega}$ obtained from wind tunnel forced oscillation results at $Re = 0.6 \times 10^6$.

IV. Tuning and Validation of Aerodynamic Model

Upset prevention and recovery training (UPRT) on modern flight simulators is one of the measures aimed at reduction of LOC-I. An important requirement in this regard is to avoid negative transfer of training, which could actually jeopardize rather than increase flight safety. This condition impose particular requirements on validation of the aerodynamic model in the extended flight envelope, where aircraft behavior can appear very unusual for untrained pilots.

There are well-developed and widely accepted objective and subjective validation tests for aerodynamic models under normal flight conditions. In contrast, the validation of aircraft post-stall dynamics faces fundamental difficulties connected with the variety of types of motion involved, such as "g-break", longitudinal self-sustained pitching oscillations and lateral-directional departures which are not precisely repeatable. Under stall conditions, an airplane can find itself in different critical flight regimes, and minor changes in control inputs can trigger a transition from one regime to another. Objective tests are limited owing to the hazardous nature of flight testing in the extended flight envelope. Subjective validation is possible, but this needs feedback from experienced pilots familiar with airplane post-stall dynamics. Meanwhile, the flight simulator constraints in motion cuing and visualization systems should not interfere with pilots' ratings for the flight simulation model itself.

Some methods of aerodynamic model tuning and validation in the extended flight envelope such as parametrised intensity of aerodynamic autorotation and post-stall gyration, adjustment of spin motion characteristics and in the end subjective validation of the post-stall dynamics by experienced pilots are discussed here.

A. Approximate Departure Criterion

Two approximate criteria are widely recognized for evaluation of combat aircraft susceptibility to loss of control and lateral-directional stability at high angles of attack [15]. They are based on the lateral control departure parameter (LCDP) and the quantity $C_{n_{\beta\text{dyn}}}$, defined as

$$\text{LCDP} = C_{n_\beta} - C_{l_\beta}\left(\frac{C_{n_{\delta_a}}}{C_{l_{\delta_a}}}\right),$$

$$C_{n_{\beta\text{dyn}}} = C_{n_\beta}\cos\alpha - \left(\frac{I_z}{I_x}\right)C_{l_\beta}\sin\alpha. \tag{8}$$
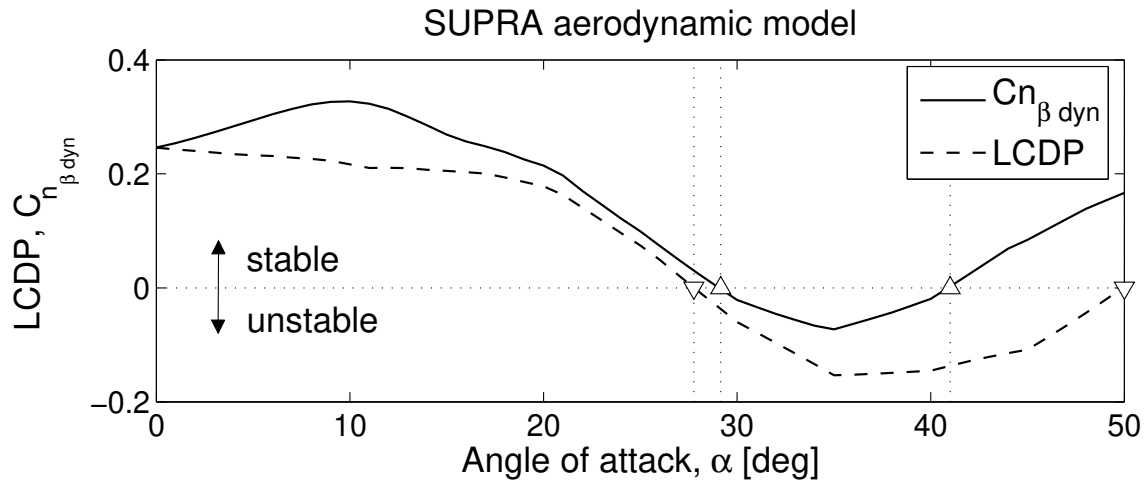
The criteria

$$\text{LCDP} < 0,$$

$$C_{n_{\beta\text{dyn}}} < 0 \tag{9}$$

then indicate reverse controllability in roll and aperiodic instability in directional motion, respectively. These criteria applied to the SUPRA model show a tendency to instability at angles of attack in the range $\alpha = 28°–50°$, which is more appropriate for spin regimes, but show no signs of instability in the range $\alpha = 10°–25°$ typical of stall conditions

(Fig. 13a). There is an obvious need for an additional criterion, reflecting the contribution of aerodynamic autorotation. Such a criterion, derived from the linearized lateral-directional equations with eliminated spiral mode, is provided by the quantity [40]

$$\sigma_\omega = C_{n_\beta} C_{l_\omega} - C_{l_\beta} C_{n_\omega}, \tag{10}$$

where the aerodynamic derivatives $C_{l\beta}$ and $C_{n\beta}$ are obtained from the wind tunnel static tests, while $C_{l\omega}$ and $C_{n\omega}$ are obtained from the rotary balance tests. Positive values, $\sigma_\omega > 0$, indicate the onset of aperiodic "conical" instability produced by aerodynamic autorotation. The dependence $\sigma_\omega(\alpha)$, calculated using aerodynamic derivatives obtained in wind tunnels at $Re = 0.6 \times 10^6$, does not indicate instability in the stall region, although its absolute magnitude drops significantly (see the solid line in Fig. 13b).

(a)
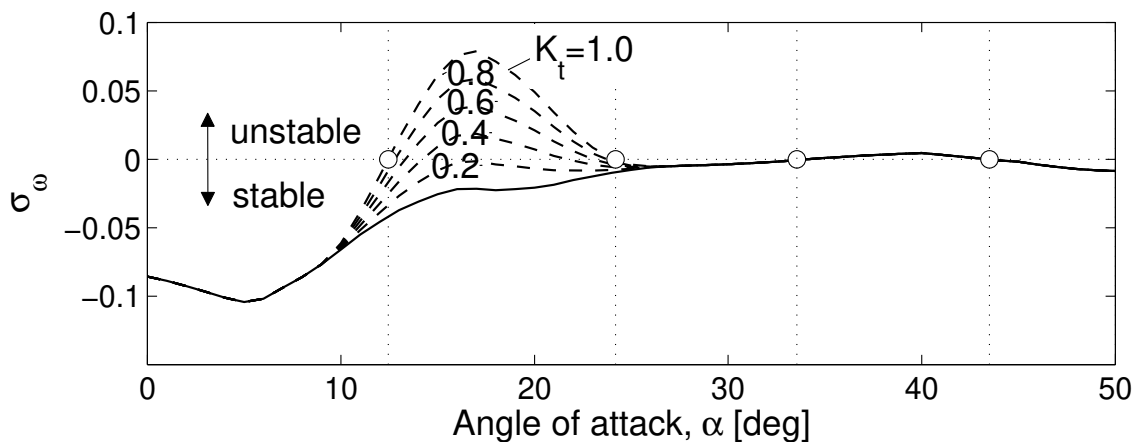
(b)

Fig. 13   Approximate departure criteria and tuning parameter k_t shaping $\sigma_\omega(\alpha)$ dependence.
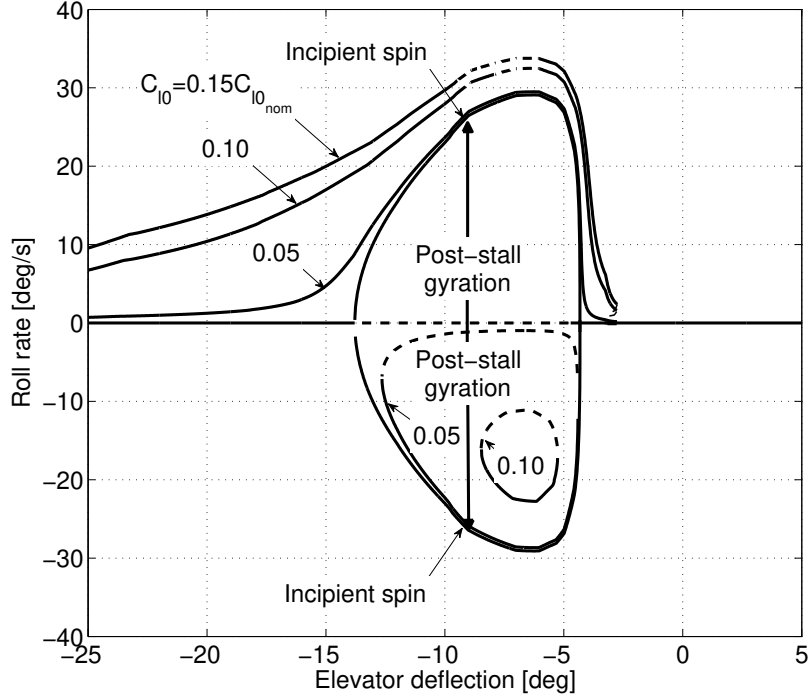
Fig. 14   Post-stall gyration and roll rate in incipient spin at $k_t = 0.4$.

The analysis of Reynolds number sensitivities from CFD simulations discussed in the previous section indicates significant levels of instability in the stall region ($10° < \alpha < 24°$). These variations offer some latitude for introducing a number of tuning parameters into the aerodynamic model within this range. For example, Fig. 13b shows a smooth transformation of the function $\sigma_\omega(\alpha)$ as the introduced tuning parameter k_t changes in the range $[0, 1]$. The intensity of "conical" instability and the width of the autorotation zone gradually increase as the tuning parameter increases from $k_t = 0.2$ to $k_t = 1$. The maximum "conical" instability is reached at the level of aerodynamic autorotation, predicted in CFD simulations at $Re = 32.6 \times 10^6$ (see the previous section).

B. Post-Stall Gyration

The post-stall gyration, the intensity of which is proportional to the level of instability $\sigma_\omega > 0$, initially saturates in the "incipient spin" (where the aerodynamic and inertia moments are in balance) and further transits to a fully developed spin (where aerodynamic and gravity forces come into balance) [15]. The equilibrium roll rates of the incipient spin in the post-stall region as function of elevator deflection for different levels of aerodynamic asymmetry in roll are shown in Fig. 14. These dependences were obtained by numerical continuation, considering the reduced system of motion equations with state vector $\mathbf{x} = (\alpha, \beta, p, q, r)'$ [40]. The solid lines represent stable equilibrium solutions and the dashed lines unstable equilibrium solutions. When $C_{l0} = 0$, post-stall gyrations to the right and to the left from the central unstable equilibria are mirror-symmetric and equally probable. A very small level of aerodynamic asymmetry in roll

makes departure to one side more probable. The maximum roll rate in the incipient spin is mostly defined by nonlinear dependences of the rolling and yawing aerodynamic moments on angular velocity ω (see Fig. 11). The characteristics of the predicted incipient spins were used for preliminary selection of the parameter k_t, which was later tuned and validated in the subsequent piloted simulations.

C. Free Spin Tests

In the case of unsuccessful upset prevention and recovery action, an airplane can transit to a fully developed spin regime characterized by high angles of attack with rotation around the vertical axis [40]. Such flight conditions, with moderate longitudinal accelerations due to centrifugal force, can be realistically reproduced on modern hexapod flight simulators, although they are not included as a mandatory part of pilot training. Given this option, the SUPRA aerodynamic model has been validated for predicting the motion of a dynamically scaled free-spinning model tested in the TsAGI vertical wind tunnel.

Fig. 15 shows variations of parameters of motion: yaw angle $\psi(t)$, angle of attack $\alpha(t)$, and sideslip $\beta(t)$ in the developed agitated spin regime. The dashed and solid lines represent experimental and simulated results, respectively. The angular rates $p(t)$, $q(t)$, $r(t)$ are numerically simulated, while control settings $\delta_e(t)$, $\delta_a(t)$, $\delta_r(t)$ were predefined and used in both the experiment and the computer simulation. There is a good agreement between the experimental and predicted time histories for the yaw angle ψ, between experimental and simulated values of the angle of attack, and also there is a similarity in characteristics of the recovery process from spin, namely the termination of rotation in ψ and reduction in the angle of attack α. The angle of attack, sideslip, and roll rate are quite oscillatory, with amplitudes $\alpha_s = 7°$, $\beta_s = 12°$, and $p_s = 1.5$ rad/s. To capture the closeness in these processes is quite difficult, because the model is thrown into the wind tunnel flow manually and there is no information about initial conditions of motion. Better prediction of the agitated spin modes will need correction of the aerodynamic derivatives $C_{i_{q_w}}$ and $C_{i_{r_w}}$ $(i = l, m, n)$, for example, by means of dependence on the nondimensional rotation rate ω.

D. Piloted Simulation

The final validation of the SUPRA aerodynamic model was made in a piloted simulation with participation of a number of experienced test and airliner pilots on three flight simulators: the centrifuge-based flight simulator Desdemona at the Netherlands Organisation for applied scientific research (TNO) and two hexapod flight simulators, GRACE at NLR and PSPK-102 at TsAGI. Feedback from the pilots on the representativeness of the airplane stall dynamics helped to tune the free parameters of the SUPRA aerodynamic model to improve its fidelity. It was stressed by several pilots that the aircraft behavior in the stall region (especially in large roll-off maneuvers) was a key innovation not present in current simulation models. The SUPRA aerodynamic model was judged to be representative for a generic transport aircraft both inside and outside the normal flight envelope and to be suitable for training applications. The detailed
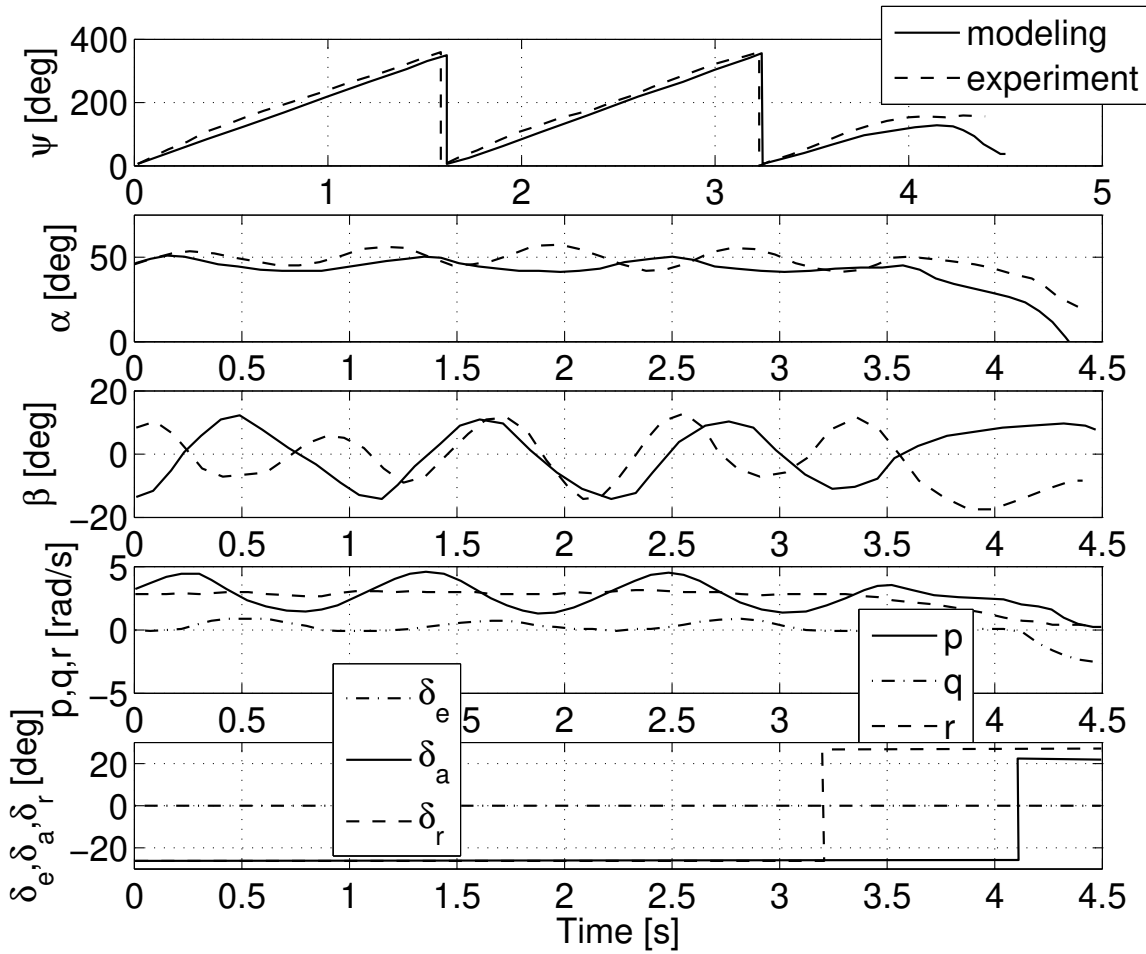
Fig. 15 Free-spin tests in the TsAGI T-105 vertical wind tunnel: experimental versus simulated results.

procedures, criteria adopted, and results obtained in the conducted validation through the piloted simulation of the SUPRA aerodynamic model are presented in [32, 33].

As an example, Fig. 16 shows the time histories and four phase portraits for the parameters of motion and control inputs from piloted simulations. These illustrate the lateral-directional departure from straight and level flight, and the development of airplane upset ($\theta = -27°$, $\phi = 98°$), followed by successful upset recovery. A visualization of the flight trajectory with airplane markers showing its orientation in 5 s intervals is presented in Fig. 17. The substantial loss of altitude $\Delta H \approx -600$ m during upset and recovery shows that such events under low-altitude flight conditions may be critically dangerous, and pilot training should be more focused on upset prevention scenarios.
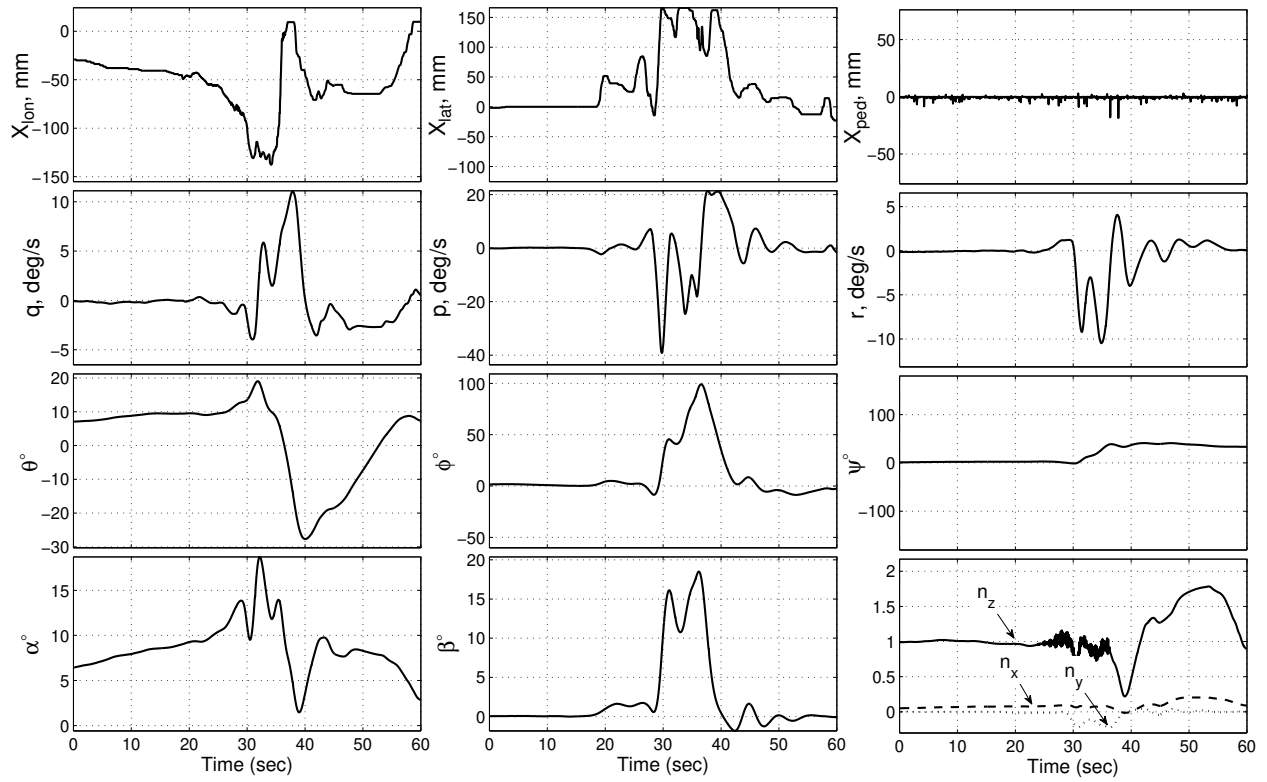
Fig. 16 Time histories and phase portraits of parameters of motion in the departure from straight and level flight.
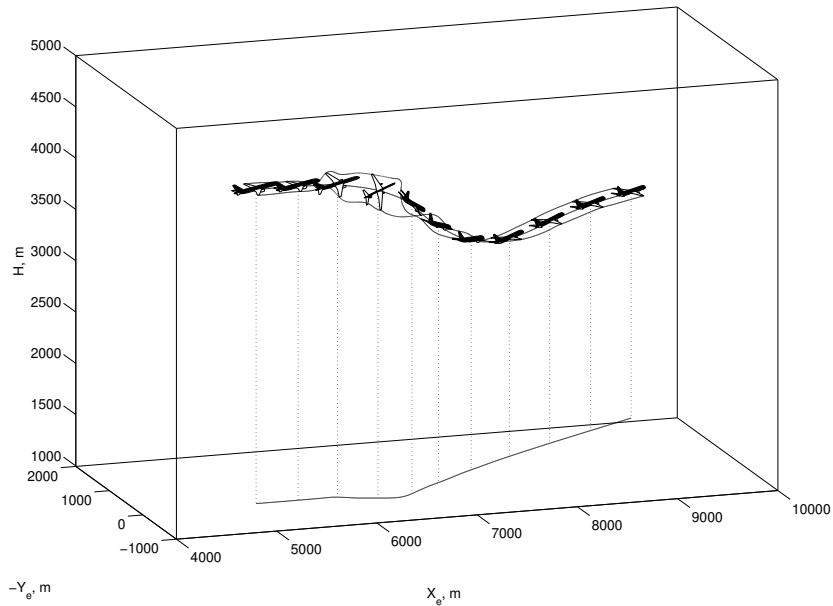
Fig. 17 Trajectory and airplane orientation during asymmetric departure and recovery.

V. Conclusions

The presented aerodynamic modeling principles for post-stall flight simulation of a generic transport airplane, which were implemented in the SUPRA aerodynamic model for an extended envelope, rely on

- consistent use of wind tunnel static, forced oscillation, and rotary balance test data and a blending procedure based on wind-axis angular rates;
- complementary CFD simulations for rotary balance type of motion under stall and post-stall conditions at high Reynolds number $Re = 32.6 \times 10^6$;
- the introduction of tunable parameters in the aerodynamic model for correction of wind tunnel data in the stall and post-stall regions;
- extensive validation of the aerodynamic model in piloted simulations by professional test and airliner pilots on hexapod and centrifuge-based flight simulator platforms.

The SUPRA aerodynamic model was rated by pilots to be representative for a generic transport aircraft both inside and outside the normal flight envelope and to be suitable for training applications.

Acknowledgements

who validated the SUPRA model, feedback from members of the expert group, the help of colleagues from TsAGI in providing the free-spin test data, and the help of Mohamed Sereez in CFD computations for the CRM wing–body configuration. The authors express special thanks to Vladimir Birukov for tuning the aerodynamic model under stall conditions.

References

[1] "Boeing: Statistical Summary of Commercial Jet Airplane Accidents. Worldwide Operations 1959-2016," *Aviation Safety Boeing Commercial Airplanes*, 2017. `www.boeing.com/news/techissues/pdf/statsum.pdf`, accessed on 15 March 2018.

[2] Schroeder, J. A., "Research and Technology in Support of Upset Prevention and Recovery Training," *AIAA Modeling and Simulation Technologies Conference*, AIAA, 2012. Paper 2012-4567.

[3] Belcastro, C. M., and Jacobson, S. R., "Future Integrated Systems Concept for Preventing Aircraft Loss-of-Control Accidents," *AIAA Guidance, Navigation, and Control Conference*, AIAA, 2010. Paper 2010-8142.

[4] "Mission statement. `http://icatee.org/mission-statement`," The International Committee for Aviation Training in Extended Envelopes (ICATEE), accessed on 15 March 2018.

[5] Singh, J., and Jategaonkar, R. V., "Identification of Lateral-Directional Behavior in Stall from Flight Data," *Journal of Aircraft*, Vol. 33, No. 3, 1996, pp. 627–630. `https://doi.org/10.2514/3.46993`.

[6] Brandon, J. M., Foster, J. V., Shah, G. H., Gato, W., and Wilborn, E., "Comparison of Rolling Moment Characteristics During Roll Oscillations for a Low and a High Aspect Ration Configuration," *AIAA Atmospheric Flight Mechanics Conference and Exhibit*, AIAA, Providence, Rhode Island, 2004. Paper 2004-5273.

[7] Foster, J. V., Cunningham, K., Fremaux, C. M., Shah, G. H., Robert, A., Rivers, E. C. S., Wilborn, J. E., and Gato, W., "Dynamics Modeling and Simulation of Large Transport Airplanes in Upset Conditions," *AIAA Guidance, Navigation, and Control Conference and Exhibit*, AIAA, 2005. Paper 2005-5933.

[8] Cunningham, K., Foster, J. V., Shah, G. H., Stewart, E. C., Ventura, R. N., Rivers, R. A., Wilborn, E. E., and Gato, W., "Simulation Study of Flap Effects on a Commercial Transport Airplane in Upset Conditions," *AIAA Atmospheric Flight Mechanics Conference and Exhibit*, AIAA, 2005. Paper 2005-5908.

[9] Murch, A. M., and Foster, J. V., "Recent NASA Research on Aerodynamic Modeling of Post-Stall and Spin Dynamics of Large Transport Airplanes," *45th AIAA Aerospace Sciences Meeting and Exhibit*, AIAA, 2007. Paper 2007-463.

[10] Murphy, P. C., and Klein, V., "Transport Aircraft System Identification from Wind Tunnel Data," *AIAA Atmospheric Flight Mechanics Conference and Exhibit*, AIAA, Honolulu, Hawaii, 2008. Paper 2008-6202.

[11] Murphy, P. C., Klein, V., and Frink, N. T., "Unsteady Aerodynamic Modeling in Roll for the NASA Generic Transport Model," *AIAA Atmospheric Flight Mechanics Conference and Exhibit*, AIAA, 2012. 2012-4652.

[12] Gringras, D. R., and Ralston, J. N., "Aerodynamics Modeling for Upset Training," *AIAA Modeling and Simulation Technologies Conference and Exhibit*, AIAA, Honolulu, Hawaii, 2008. Paper 2008-6870.

[13] Abramov, N., Goman, M., Khrabrov, A., and Soemarwoto, B., "Aerodynamic model development for simulation of upset recovery of transport airplane," *RAeS Aerodynamics Conference 2010: Applied Aerodynamics: Capabilities and Future Requirements*, Bristol, UK, 2010.

[14] Abramov, N., Goman, M., Khrabrov, A., Kolesnikov, E., Fucke, L., Soemarwoto, B., and Smaili, H., "Pushing Ahead - SUPRA Airplane Model for Upset Recovery," *AIAA Modeling and Simulation Technologies Conference*, AIAA, Mineapolis, Minesota, 2012. Paper 2012-4631.

[15] "Manoeuvre Limitations of Combat Aircraft," Advisory Report 155A, AGARD, August 1979.

[16] "Rotary-Balance Testing for Aircraft Dynamics," Advisory Report 265, AGARD, 1990.

[17] "Cooperative Programme on Dynamic Wind Tunnel Experiments for Manoeuvrable Aircraft," Advisory Report 305, AGARD, October 1996.

[18] Kalviste, J., "Use of Rotary Balance and Forced Oscillation Test Data in a Six Degrees of Freedom Simulation," *AIAA 9th Atmospheric Flight Mechanics Conference*, AIAA, San Diego, California, 1982. Paper 82-1364.

[19] Chambers, J. R., "Modeling flight: the role of dynamically scaled free-flight models in support of NASA's aerospace programs," SP 2009-575, NASA, 2009. ISBN 978-0-16-084633-5.

[20] Ericsson, L. E., and Reding, J. P., "Dynamic Stall Analysis in Light of Recent Numerical and Experimental Results," *Journal of Aircraft*, Vol. 13, No. 4, 1976, pp. 248–255.

[21] "NASA Common Research Model," `https://commonresearchmodel.larc.nasa.gov`, accessed on 15 March 2018.

[22] Vassberg, J. C., DeHaan, M. A., Rivers, S. M., and Wahls, R. A., "Development of a Common Research Model for Applied CFD Validation Studies," *26th AIAA Applied Aerodynamics Conference*, AIAA, Honolulu, Hawaii, 2008. Paper 2008-6919, `https://doi.org/10.2514/6.2008-6919`.

[23] Boerstoel, J. W., Kassies, A., Kok, J. C., and Spekreijse, S. P., "ENFLOW, a full-functionality system of CFD codes for industrial Euler/Navier-Stokes flow computations," Tech. rep., NLR TP 96286U, 1996.

[24] Laban, M., Kok, J. C., and Prananta, B. B., "Numerical tools for contra-rotating open-rotor performance, noise and vibration assessment," *27th Congress of the International Council of the Aeronautical Sciences*, Nice, France, 2010.

[25] Goman, M., and Khrabrov, A., "State-space representation of aerodynamic characteristics of an aircraft at high angles of attack," *Journal of Aircraft*, Vol. 31, No. 5, 1994, pp. 1109–1115. `https://doi.org/10.2514/3.46618`.

[26] Greenwell, D., "A Review of Unsteady Aerodynamic Modelling for Flight Dynamics of Manoeuvrable Aircraft," *AIAA Atmospheric Flight Mechanics Conference and Exhibit*, AIAA, Providence, Rhode Island, 2004. Paper 2004-5276, (`https://doi.org/10.2514/6.2004-5276`).

[27] Khrabrov, A., Vinogradov, Y., and Abramov, N., "Mathematical Modelling of Aircraft Unsteady Aerodynamics at High Incidence with Account of Wing-Tail Interaction," *AIAA Atmospheric Flight Mechanics Conference and Exhibit*, AIAA, Providence, Rhode Island, 2004. Paper 2004-5278, `https://doi.org/10.2514/6.2004-5278`.

[28] Abramov, N., Goman, M., and Khrabrov, A., "Aircraft Dynamics at High Incidence Flight with Account of Unsteady Aerodynamic Effects," *AIAA Atmospheric Flight Mechanics Conference and Exhibit*, AIAA, Providence, Rhode Island, 2004. Paper 2004-5274, `https://doi.org/10.2514/6.2004-5274`.

[29] Luchtenburg, D. M., Rowley, C. W., Lohry, M. W., Martinelli, L., and Stengel, R. F., "Unsteady High-Angle-of-Attack Aerodynamic Models of a Generic Jet Transport," *Journal of Aircraft*, Vol. 52, No. 3, 2015, pp. 890–895. `https://doi.org/10.2514/1.C032976`.

[30] "Simulation of UPset Recovery in Aviation (SUPRA), `http://www.supra.aero`," Research project funded by the 7th Framework Programme of the European Commission, accessed on 27 March 2018.

[31] Gubanova, M., Bragin, N., Perchenkov, E., and Slitinskaya, A., "High-Lift System Design by Numerical Methods and Wind Tunnel Verification," *29th Congress of the International Council of the Aeronautical Sciences*, St. Petersburg, Russia, 2014.

[32] Nooij, S. A. E., Wentink, M., Smaili, H., Zaichik, L., and Groen, E. L., "Motion Simulation of Transport Aircraft in Extended Envelopes: Test Pilot Assessment," *Journal of Guidance, Control, and Dynamics*, Vol. 40, No. 4, 2017. `https://doi.org/10.2514/1.G001790`, pp. 776–788.

[33] Ledegang, W. D., and Groen, E. L., "Stall Recovery in a Centrifuge-Base Flight Simulator With an Extended Aerodynamic model," *The International Journal of Aviation Psychology*, Vol. 25, No. 2, 2015, pp. 122–140. `https://dx.doi.org/10.1080/10508414.2015.1131085`.

[34] Fucke, L., Biryukov, V., Grigoryev, M., Rogozin, V., Groen, E., Wentink, M., Field, J., Soemarwoto, B., Abramov, N., Goman, M., and Khrabrov, A., "Developing Scenarios for Research into Upset Recovery Simulation," *AIAA Modeling and Simulation Technologies Conference*, AIAA, Toronto, Ontario Canada, 2010. Paper 2010-7794, `https://doi.org/10.2514/6.2010-7794`.

[35] Tristrant, D., and Beyers, M. E., "Oscillatory coning. Chapter 4 in Rotary-Balance Testing for Aircraft Dynamics," Advisory Report 265, AGARD, 1990.

[36] Pattinson, J., Lowenberg, M., and Goman, M., "Multi-Degree-of-Freedom Wind-Tunnel Maneuver Rig for Dynamic Simulation and Aerodynamic Model Identification," *Journal of Aircraft*, Vol. 50, No. 2, ????, pp. 551–566. Paper 2008-6919, `https://doi.org/10.2514/1.C031924`.

[37] Vassberg, J., "A Unified Baseline Grid about the Common Research Model Wing-Body for the Fifth AIAA CFD Drag Prediction Workshop," *29th AIAA Applied Aerodynamics Conference, Fluid Dynamics and Co-located Conferences*, AIAA, Honolulu, Hawaii, 2011. Paper 2011-3508, `https://doi.org/10.2514/6.2011-3508`.

[38] Menter, F. R., "Two-Equation Eddy-Viscosity Turbulence Models for Engineering Applications," *AIAA Journal*, Vol. 32, No. 8, 1994, pp. 1598–1605.

[39] Soemarwoto, B. I., Nugroho, A., Baalbergen, E. H., and Aribowo, A., "CFD-based collaborative design optimization using eCFD," *29th Congress of the International Council of the Aeronautical Sciences*, ICAS, St. Petersburg, Russia, 2014, pp. pp.885–995. ICAS2014-0739.

[40] Goman, M. G., Zagainov, G. I., and Khramtsovsky, A. V., "Application of Bifurcation Methods to Nonlinear Flight Dynamics Problems," *Progress in Aerospace Sciences*, Vol. 33, No. 9-10, 1997, pp. 539–586. `https://doi.org/10.1016/S0376-0421(97)00001-8`.